

Segmentation of mid-ocean ridges attributed to oblique mantle divergence

Brandon P. VanderBeek^{1*}, Douglas R. Toomey¹, Emilie E. E. Hooft¹ and William S. D. Wilcock²

The origin of mid-ocean ridge segmentation—the systematic along-axis variation in tectonic and magmatic processes—remains controversial. It is commonly assumed that mantle flow is a passive response to plate divergence and that between transform faults magma supply controls segmentation. Using seismic tomography, we constrain the geometry of mantle flow and the distribution of mantle melt beneath the intermediate-spreading Endeavour segment of the Juan de Fuca Ridge. Our results, in combination with prior studies, establish a systematic skew between the mantle-divergence and plate-spreading directions. In all three cases studied, mantle divergence is advanced with respect to recent changes in the plate-spreading direction and the extent to which the flow field is advanced increases with decreasing spreading rate. Furthermore, seismic images show that large-offset, non-transform discontinuities are regions of enhanced mantle melt retention. We propose that oblique mantle flow beneath mid-ocean ridges is a driving force for the reorientation of spreading segments and the formation of ridge-axis discontinuities. The resulting tectonic discontinuities decrease the efficiency of upward melt transport, thus defining segment-scale variations in magmatic processes. We predict that across spreading rates mid-ocean ridge segmentation is controlled by evolving patterns in asthenospheric flow and the dynamics of lithospheric rifting.

Since the discovery that Earth's mid-ocean ridge system is divided into segments¹⁻³ a wealth of observations have shown that there are systematic, along-axis variations in tectonic and magmatic processes^{2,4-6}. Between transform faults, the boundaries of ridge segments are defined by long-lived, non-transform tectonic offsets or second-order ridge crest discontinuities^{2,3} (Fig. 1) that often occur at axial depth maxima and that migrate along the plate boundary. These second-order discontinuities include overlapping spreading centres (OSCs) at fast- and intermediate-spreading rates, and oblique shear zones at slow-spreading rates. The origin of non-transform tectonic offsets and their relations to segment-scale magmatic processes remains actively debated^{1,2,5-9}.

The prevailing hypothesis for segmentation of spreading centres attributes second-order offsets to variations in magma supply from the upwelling mantle. In this view, segment centres overlie sites of increased melt supply and magma is redistributed along axis at crustal or mantle depths toward magma-starved segment ends^{1,2,8,10}. Alternatively, competing hypotheses suggest that changes in the plate-spreading direction are related to the formation of tectonic offsets⁷ and to a misalignment between sub-ridge mantle and crustal processes⁹. Here, we seismically image the geometry of mantle flow and the distribution of shallow mantle melt beneath the intermediate-spreading Endeavour segment of the Juan de Fuca Ridge (JdFR). We synthesize our results with observations from other spreading environments to identify the mechanisms responsible for tectonic and magmatic segmentation of the midocean ridge system.

Experiment geometry and tomographic imaging

Figure 2 shows the location of seismic sources and receivers used to construct our tomographic model of the shallow mantle beneath the Endeavour segment of the JdFR. We use arrival times of seismic energy refracted beneath the Mohoroviči (Moho) discontinuity

(Pn arrivals) to image the upper $4\,\mathrm{km}$ of the mantle within an area extending $20\,\mathrm{km}$ by $100\,\mathrm{km}$ in the cross- and along-axis directions, respectively. Over 5,000 Pn arrivals provide excellent sampling of mantle structure and previous studies^{11,12} provide a three-dimensional (3D) starting model of crustal velocity and thickness (see Methods).

The Pn delay times plotted by azimuth show a $\cos 2\theta$ -pattern, which is indicative of azimuthal seismic anisotropy (Fig. 3). The azimuth of the fast axis of mantle anisotropy is $122^{\circ} \pm 1^{\circ}$ and the magnitude is $4.7 \pm 0.4\%$ (see Methods). The azimuth of anisotropy is rotated 12° clockwise from the predicted plate-spreading direction¹³. Examination of subsets of Pn data do not show evidence for along-axis variations in anisotropic structure (see Methods).

Our preferred tomographic solution is shown in Fig. 2b; the Methods section discusses model resolution, sensitivity and tradeoffs. The isotropic component of mantle velocity is anomalously low along the entire length of the Endeavour segment. However, the trend of the mantle low-velocity zone (MLVZ) does not follow the Endeavour Ridge axis, nor is it rotated clockwise with respect the ridge segment (that is, perpendicular to the fast axis of mantle anisotropy), but instead connects the OSCs. Remarkably, both the cross-axis width and amplitude of the MLVZ are largest beneath the segment-bounding Cobb and Endeavour OSCs. Beneath the Cobb OSC the MLVZ is ~30 km in diameter, centred west of the eastern spreading limb, and the lowest mantle velocities $(\sim 7.1 \text{ km s}^{-1})$ are beneath the eastern rift. At the Endeavour OSC, a 30-km-wide MLVZ extends across both spreading limbs with the lowest velocities (~7.1 km s⁻¹) concentrated beneath the western rift. By contrast, the MLVZ beneath the main Endeavour Ridge, where a nearly continuous crustal axial magma lens has been identified¹⁴, is a narrower (~15 km), more linear feature characterized by slightly higher velocities (\sim 7.4 km s⁻¹). Three local

¹Department of Geological Sciences, University of Oregon, Eugene, Oregon 97403, USA. ²School of Oceanography, University of Washington, Seattle, Washington 98195, USA. *e-mail: brandonv@uoregon.edu

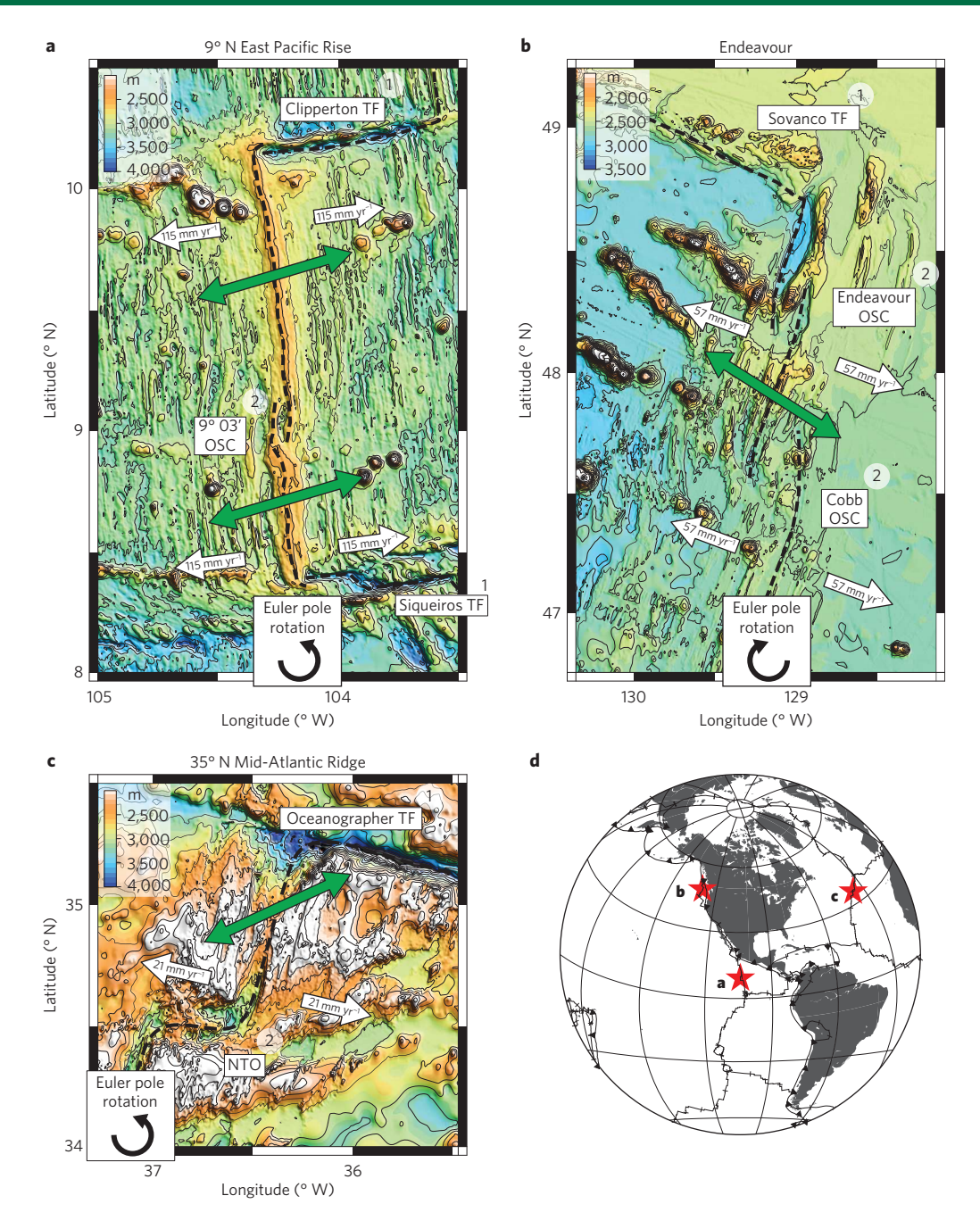


Figure 1 | Tectonic segmentation of fast-, intermediate- and slow-spreading ridges. a-c, Bathymetric maps of the EPR (a), the Endeavour region of the JdFR (b) and the MAR (c). The dashed lines show plate boundaries. Transform faults (TF), overlapping spreading centres (OSC) and non-transform offsets (NTO) are labelled; numbers indicate order of a tectonic discontinuity². The white arrows show the spreading direction and full-spreading rate¹³. The green arrows indicate the azimuth of seismic anisotropy for the EPR⁹, JdFR (this study) and MAR²¹. Recent rotations in the Euler pole of each plate system²²⁻²⁴ are indicated. **d**, Map showing regional location of ridge segments (red stars).

minima punctuate the central MLVZ at intervals of \sim 15 km. The southern- and northern-most of these minima are located \sim 5 km off axis.

Mantle flow and melt distribution at Endeavour

The anisotropic component of our model constrains the segmentscale geometry of uppermost mantle flow. This is because seismic anisotropy in the mantle is dominated by the lattice-preferred orientation of olivine crystals¹⁵. In response to strain induced by gradients in the mantle flow field, the crystallographic *a* axis of olivine (the fast axis of P-wave propagation) aligns parallel to the direction of maximum shear¹⁶. As mantle divergence generates large shear strains¹⁷, we infer that the azimuth of seismic anisotropy parallels the mantle-divergence direction, which is skewed 12° clockwise from the plate-spreading direction. Furthermore, the observed $\cos 2\theta$ -pattern (Fig. 3) is consistent with a 2D flow field and does not suggest segment-scale, 3D flow consistent with diapiric upwelling¹⁸.

The isotropic component of our model constrains the thermal structure and distribution of melt beneath the Endeavour segment. To explain the magnitude of the MLVZ with thermal perturbations alone requires unrealistically large temperature anomalies (see Supplementary Information). The seismic velocity reduction unaccounted for by a likely thermal anomaly is consistent

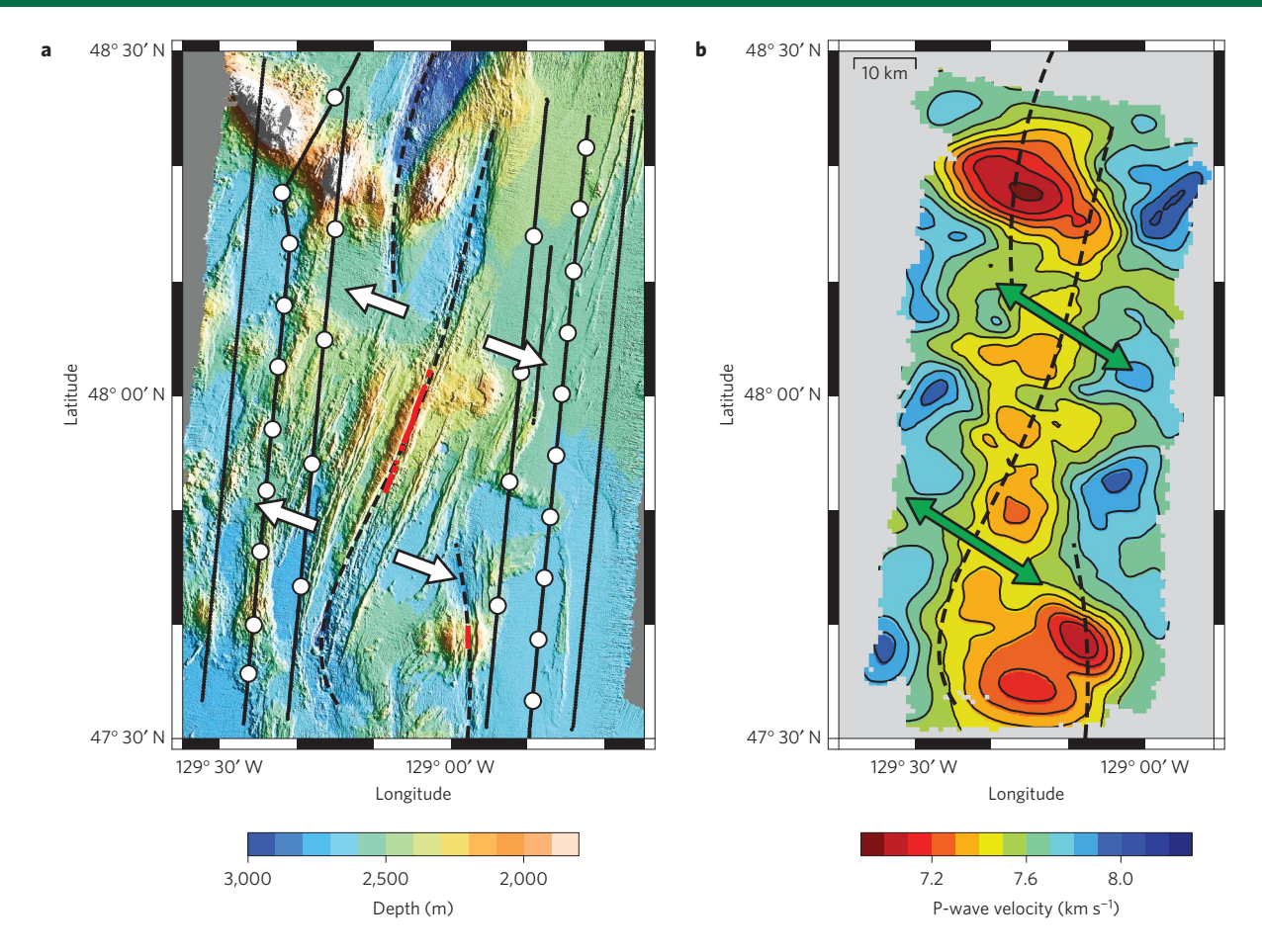


Figure 2 | **Location and geometry of the ETOMO experiment and tomographic image of the mantle velocity structure. a**, Bathymetric map of the Endeavour Ridge. Black dots and white circles show the location of seismic sources and receivers, respectively (see Methods). The white arrows indicate the plate-spreading direction¹³. The location of the crustal axial magma lens is shown in red¹⁴. **b**, Tomographic image of the mantle P-wave velocity structure at 7.8 km depth beneath the seafloor; contour interval is 0.1 km s⁻¹. The green arrows indicate the azimuth of seismic anisotropy. The dashed lines identify the plate boundary.

with $<\!2\%$ partial melt beneath the segment centre and 1 to 5% beneath the OSCs (see Supplementary Information). Given the seismic wavelength of Pn, the partially molten regions must extend several kilometres beneath the Moho, although the details of melt geometry are not constrained by our data. We infer that the MLVZ defines the segment-scale geometry of the shallow mantle magmatic system.

Our results indicate that the greatest volumes of mantle melt are currently beneath the second-order tectonic discontinuities. The observed seismic velocities are consistent with as much as 90 km³ of melt within the upper 4 km of the mantle beneath each OSC (see Supplementary Information). In comparison, we estimate that up to 40 km³ of melt is present within the upper 4 km of the mantle beneath the non-overlapping portion of the Endeavour Ridge or less than half that present beneath either OSC. Several studies suggest that the inferred segment-scale melt distribution is not related to nearby seamount chains (see Supplementary Information). In contrast to the estimated melt volumes, crustal thickness along the Endeavour segment, which constrains the time-integrated magma supply, is greatest at the segment centre^{12,19}. To reconcile the current distribution of mantle melt with the time-averaged supply, we infer that mantle melt is efficiently extracted beneath the segment centre and that greater amounts of melt are stored within the mantle beneath tectonic offsets. Additional evidence supporting this inference is discussed below.

We note that the MLVZ does not align with the Endeavour Ridge axis, nor is it perpendicular to the mantle-divergence direction as

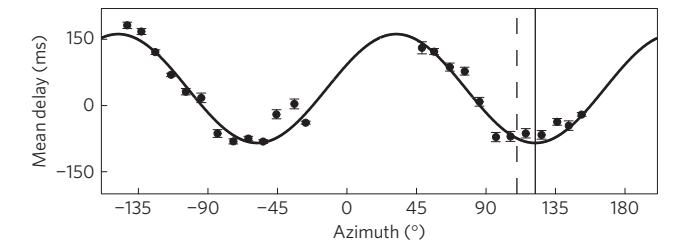


Figure 3 | Mean Pn delay times versus azimuth. Delays are calculated relative to an isotropic mantle (7.6 km s⁻¹), binned at 10° intervals, and corrected to 40 km range (see Methods). The error bars show the 95% confidence interval in the mean delay time as determined by a Student's *t*-test. The solid line is the best-fit cos 2θ -curve. The azimuth of seismic anisotropy is $122^{\circ}\pm1^{\circ}$ (solid vertical line), which is rotated 12° clockwise from the plate-spreading direction¹³ (vertical dashed line). The anisotropic magnitude is $4.7\pm0.4\%$.

is the case for the fast-spreading East Pacific Rise (EPR)⁹. Instead, the MLVZ lies sub-parallel to the regional, north-south trend of the northern JdFR, a result consistent with the focusing of shallow mantle melt beneath the youngest and thinnest lithosphere²⁰. Indeed, as discussed below, cross- and along-axis variations in thermal structure appear to be the primary factor influencing the segment-scale distribution of magma at both sub-Moho and crustal depths.

Tectonic segmentation of mid-ocean ridges

Seismic studies from fast-9, intermediate- (this study), and slowspreading²¹ centres reveal a remarkable characteristic of the mid-ocean ridge system: a systematic skew between the plateand mantle-divergence directions, where the magnitude of skew increases as spreading rate decreases (Fig. 4). Furthermore, for each region studied, the skew of mantle divergence is in the same direction as, and ahead of, recent changes in the spreading direction (Fig. 1). Along both the 9° N EPR and 35° N Mid-Atlantic Ridge (MAR) segments, the mantle flow field is rotated in an anticlockwise sense and the associated Euler poles have progressed anticlockwise over the last several million years^{22,23}. Similarly, we find that mantle flow beneath the Endeavour is skewed clockwise and the Pacific-JdF plate boundary has been reorganizing clockwise over the last ~10 Myr (ref. 24). These observations indicate that sub-ridge mantle dynamics are not solely a passive response to overlying plate motion. On the basis of these results, we assume that current plate-spreading directions are lagging behind a more rapidly evolving asthenospheric flow field, and that this lag increases with decreasing spreading rate (Fig. 4).

We propose that skew between asthenospheric flow and plate motions generates a drag force on the base of oceanic lithosphere that contributes to changes in spreading direction and the formation of second-order tectonic discontinuities. Basal shear stresses may be small, but they can amount to a significant force when integrated over a substantial area ($\sim 10^{14-16}$ N assuming strain rates of 10^{-15} s⁻¹, asthenosphere viscosity of 10¹⁹ Pa s, and plate area of 10^{10–12} m²). In support of this view, shear wave splitting observations made at sites throughout the JdF plate are consistent with a clockwise rotation of asthenospheric flow relative to absolute plate motion²⁵. A skewed mantle flow field would generate transtensional stresses at the ridge. We thus suggest that ridge segments and second-order tectonic offsets are analogous to the formation of transtensional cracks. In a transtensional stress regime, left- or right-stepping offsets will form in right- or left-lateral shear, respectively²⁶. For numerous second-order discontinuities across a range of spreading rates—including the sections of the EPR, JdFR and MAR discussed here—the formation and geometry of segment offsets correlate with recent changes in spreading direction²⁷. We hypothesize that these changes in spreading direction are in part a response to skew between plate motions and mantle flow and that the work required to reorient transpressive oceanic transform faults limits the rate at which spreading directions can change9. For a given spreading rate, a range of skew magnitudes may be present depending on the tectonic history and geometry of bounding firstorder discontinuities. However, since transform faults occur more frequently along more slowly spreading regions of the mid-ocean ridge system, we predict that the magnitude of skew will, on average, increase with decreasing spreading rate.

Magmatic segmentation of mid-ocean ridges

Tomographic imaging of the topmost mantle from fast- and intermediate-spreading ridges reveals a second remarkable characteristic of the mid-ocean ridge system: second-order tectonic offsets are sites of increased storage of shallow mantle melt over relatively broad areas. At the Endeavour segment both the cross-axis width and magnitude of the MLVZ are greatest beneath the segment-bounding OSCs (Fig. 2b). Similarly, tomographic results from the EPR reveal a MLVZ that is both more pronounced and laterally extensive beneath the 9° 03′ N OSC9. These observations cannot be attributed to an increase in magma supply. This is because geophysical studies show that second-order offsets along the EPR^{28,29} and the JdFR^{12,30} are regions of normal or decreased crustal thickness. In addition, isotopic variations in axial basalts from the 9° 03′ N OSC show no evidence for variations in extents of melting near the discontinuity³¹.

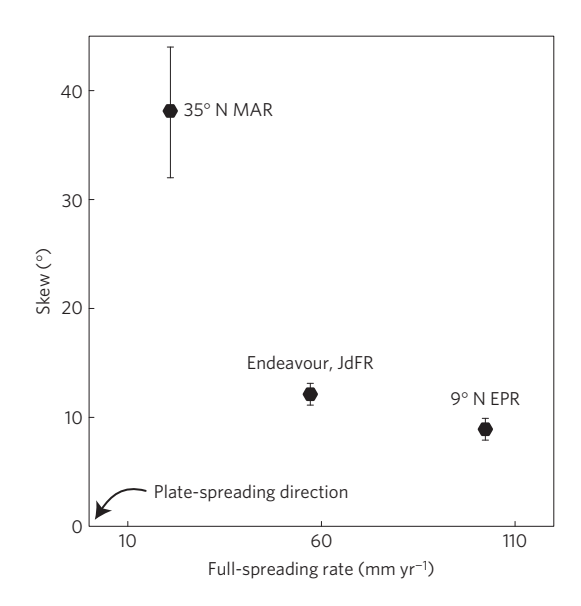


Figure 4 | Skew of mantle anisotropy by spreading rate. The magnitude of the skew between mantle anisotropy and the predicted plate-spreading direction¹³ is plotted by spreading rate; uncertainties are defined by the standard error in the weighted least-squares fit to Pn travel-time residuals from each experiment. Observations from the EPR and MAR are taken from refs 9,11, respectively.

We propose a model for the magmatic segmentation of fastand intermediate-spreading centres based on the hypothesis that the segment-scale characteristics of the shallow mantle and crustal magmatic systems are governed by the pattern of rifting and resulting near-axis thermal structure (Fig. 5); the implications of our model for slow-spreading ridges are discussed below. Away from the influence of hot spots, we assume that the production of mantle melt is uniform at the scale of second-order ridge segments³², including their non-transform discontinuities, and that melt ascends toward the base of young lithosphere, where it is focused by sloping isotherms²⁰. In between tectonic offsets where plate separation is accommodated by a single rift-mantle melts are focused toward a discrete, well-defined plate boundary (Fig. 5a,b). Here, magma is more frequently injected into the rift and hydrothermal processes shape a narrow crustal magmatic system18, the depth of which depends on spreading rate and the efficiency of advective heat removal³³. In contrast, near secondorder tectonic offsets (Fig. 5a,c) the available mantle-derived melts are distributed between overlapping spreading limbs. This dispersal of a fixed amount of heat results in a deeper crustal magmatic system and a broader region of elevated temperatures at both lower crustal and shallow mantle depths. We assert that these conditions result in less efficient delivery of melt to mid-crustal reservoirs and the preferential retention of melt for longer periods of time at mantle depths. The consequences of longer magma residence times beneath second-order discontinuities are several, including increased magmatic differentiation at higher pressures, decreased crustal thickness beneath tectonic discontinuities, and the generation of a denser crustal unit³⁴ (Fig. 5a). Such trends are well documented along the mid-ocean ridge $\bar{\text{system}}^{4,12,28-31,34,35}.$

Our model of magmatic segmentation, coupled with the mechanics of OSC propagation, also explains the occurrence of relatively thick, dense crust behind the wake of a propagating discontinuity^{28–30,34} (Fig. 5a). Previous studies indicate that OSC propagation is not continuous, but occurs in discrete jumps, with the propagating limb rapidly lengthening and curving inward toward the basin while the failing limb is rafted off axis or recedes^{2,36,37}. Thus, the advancing limb will tap an additional source

ARTICLES

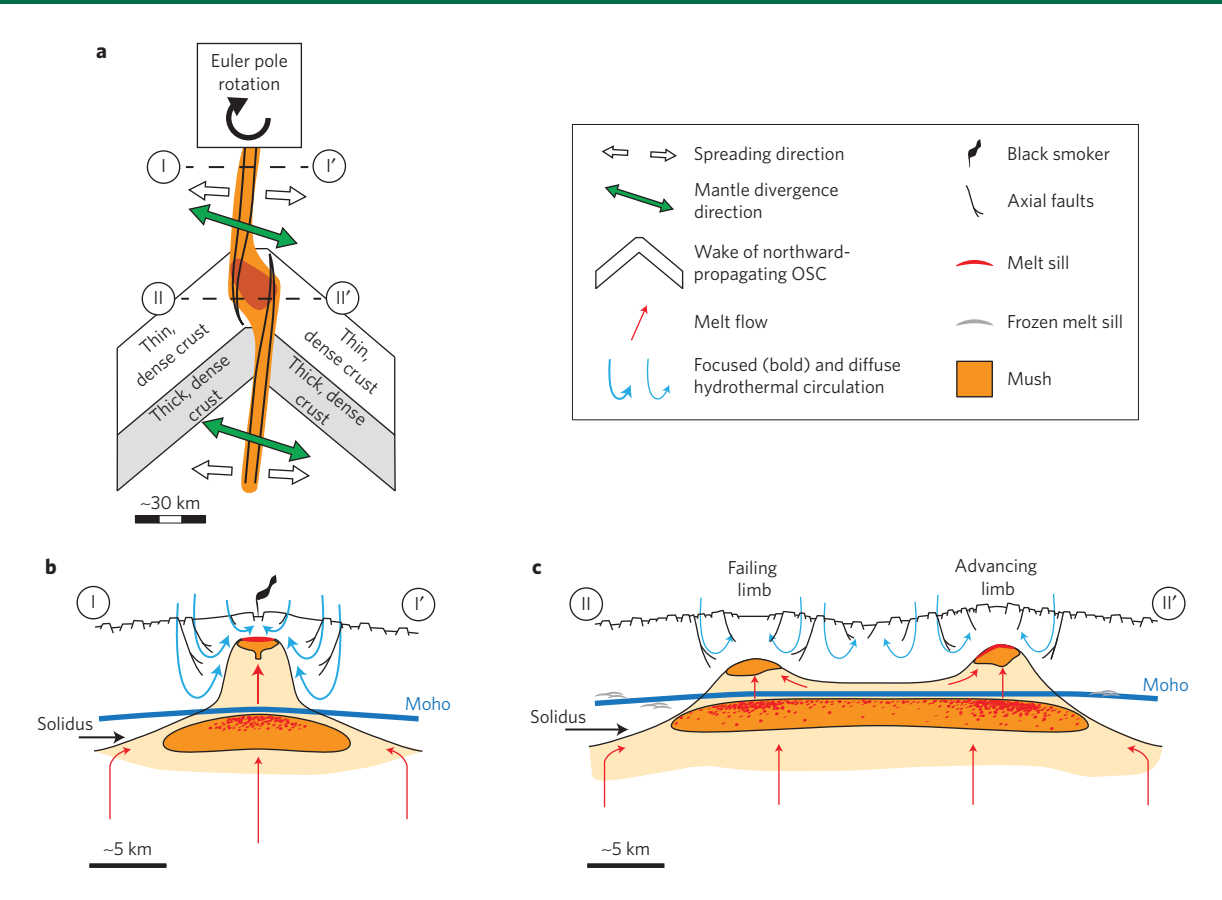


Figure 5 | Proposed model of magmatic segmentation for fast- and intermediate-spreading ridges. a, Map view of second-order ridge segments and predictions for the geometry of mantle flow, distribution of shallow mantle melt and patterns in crustal structure. The dashed lines show the cross-sections in b and c. b, Rise-perpendicular section away from a second-order, tectonic discontinuity (modified from ref. 9). c, Rise-perpendicular section across a second-order OSC; see text for discussion. The red stippling denotes regions of increased melt fraction. Seafloor relief and thickness of melt sills are exaggerated.

of mantle melt, one that has been trapped between overlapping spreading limbs and undergone greater amounts of differentiation at sub-Moho pressures. As a result, relatively thick and dense crust will be generated immediately behind the wake of a propagating OSC (Fig. 5a).

A number of studies are consistent with our assertion that mantle melt is preferentially stored and broadly distributed beneath secondorder discontinuities. Seismic imaging analyses of crustal structure along the EPR38 and Lau Spreading Centre39 identify anomalously broad axial magmatic systems spanning OSCs, similar to that depicted in Fig. 5c. Multichannel seismic imaging experiments from both the Lau Basin⁴⁰ and the EPR⁵ also reveal that widespread crustal melt lenses are characteristic of these OSCs. In contrast, away from tectonic discontinuities crustal magmatic systems are confined to relatively narrow regions centred beneath the plate boundary^{18,39} and these systems are capped by relatively narrow axial magma lenses^{40,41} (see Fig. 5b). We attribute the observed increase in the width of crustal magmatic systems near second-order offsets to vertical transport of magma from laterally extensive regions of melt accumulation at shallow mantle depths. The identification of frozen sub-Moho magma lenses found in association with migrating offsets on the JdFR⁴² and the prevalence of Moho-depth melt sills near the 9° 03′ N OSC on the EPR⁴³ further supports our interpretation that second-order discontinuities are sites of enhanced mantle melt storage. The maximum depth extent of the inferred region of melt storage must extend for several kilometres given the seismic wavelength of Pn phases. Deeper mantle imaging (10-30 km sub-Moho) of multiple non-transform discontinuities along the Lau Spreading Centre reveals that the melt production region is

uninterrupted across multiple ridge offsets⁴⁴. Assuming these results are characteristic of other spreading centres, we conclude that the retention of mantle melt beneath second-order offsets occurs within the top few kilometres of the mantle.

For slow-spreading ridges our model of magmatic segmentation also predicts that the distribution of shallow mantle melt is influenced by the geometry of tectonic segmentation. As the spreading rate decreases, the morphologic expression of second-order offsets changes from OSCs to oblique shear zones or non-transform offsets (Fig. 1) and the near-axis thermal structure will differ significantly. For example, the increased age offset at the ends of slow-spreading segments results in a thicker axial lithosphere and significant variations in the predicted along-axis mantle temperature⁴⁵. Thickened axial lithosphere will also inhibit the extraction of mantle melts⁴⁶ and promote the migration of melt towards segment centres where the lithosphere is predicted to be thinnest⁴⁷. Consequently, along-axis variations in crustal thickness are pronounced with the thickest crust located mid-segment^{21,32}.

Between second-order tectonic discontinuities the results of seismic studies show that as the spreading rate decreases the distribution of shallow mantle melt is increasingly influenced by the segment-scale thermal structure of newly formed lithosphere. At the fast-spreading EPR, where cross- and along-axis variations in thermal structure are least pronounced for the global ridge system, both the azimuth of seismic anisotropy relative to the spreading direction and the trend of the MLVZ with respect to the rise axis are skewed coherently by similar amounts 9 . Furthermore, centres of mantle melt delivery are spaced at intervals of $\sim 25 \, \mathrm{km}$ (ref. 9) and frequently occur midway between volcanic or third-order discontinuities 2,4,9,48 .

NATURE GEOSCIENCE DOI: 10.1038/NGE02745 ARTICLES

At the EPR, the cross-axis offset between a centre of mantle melt delivery and the rise axis also correlates with the intensity of rise crest volcanic, hydrothermal and tectonic activity⁹, and the distal ends of third-order segments may be associated with a decrease in the efficiency of mantle melt extraction⁴⁹.

In contrast, a coherent skew of both seismic anisotropy and the MLVZ-and by inference the direction of mantle divergence and the segment-scale shallow mantle magmatic system—is not present beneath either the JdFR or the MAR²¹. Instead, in each instance the mantle-divergence direction is skewed with respect to the platespreading direction, but the segment-scale trend of the MLVZ is either sub-parallel to that of the youngest and thinnest lithosphere (JdFR) or preferentially localized beneath segment centres where lithosphere is also predicted to be thinnest^{21,32,46} (MAR). These results suggest that 3D, segment-scale variations in the thickness of near-ridge lithosphere govern the distribution of shallow mantle melt. We note that third-order segmentation is poorly defined at the Endeavour segment⁵⁰ and not identifiable along the MAR⁶. We speculate that only in regions where along- and cross-axis variations in near-ridge lithospheric structure are minimal (for example, EPR), will there be a relation between centres of mantle magma supply and third-order segmentation.

Detailed geophysical studies of individual spreading segments support a new view of the mid-ocean ridge system in which skewed asthenospheric flow contributes to plate boundary reorganization. The resulting changes in relative plate motion are accommodated through the formation and migration of tectonic offsets. These tectonic discontinuities in turn perturb the axial thermal structure thus defining shallow mantle and crustal magmatic segmentation. This view stands in contrast to the long-standing hypothesis that mid-ocean ridge morphology reflects variations in mantle magma supply from a passively driven asthenosphere. Our results have several implications for ridge dynamics. At the scale of individual spreading segments, seismic images of the uppermost mantle indicate that crustal production is not solely a function of melt availability. Rather, the dynamics of lithospheric rifting ultimately control the transfer of mass between Earth's interior and the seafloor. On the global scale, our results indicate that tectonic segmentation across spreading rates shares a common origin related to evolving patterns of asthenospheric flow. In this view, second-order tectonic discontinuities result from the transmission of viscous stresses from the asthenosphere to the lithosphere. We speculate that the variability in the lengths of second-order ridge segments and the geometry of their bounding offsets may reflect changes in the strength of axial lithosphere as a function of spreading rate. Furthermore, we attribute the origin of skewed asthenospheric flow beneath ridges to the global mantle flow field, which is largely driven by sinking of oceanic lithosphere at subduction zones.

Methods

Methods, including statements of data availability and any associated accession codes and references, are available in the online version of this paper.

Received 20 November 2015; accepted 20 May 2016; published online 27 June 2016

References

- Schouten, H., Klitgord, K. D. & Whitehead, J. A. Segmentation of mid-ocean ridges. *Nature* 317, 225–229 (1985).
- Macdonald, K. C. et al. A new view of the mid-ocean ridge from the behaviour of ridge-axis discontinuities. Nature 335, 217–225 (1988).
- Sempéré, J. C., Purdy, G. M. & Schouten, H. Segmentation of the Mid-Atlantic Ridge between 24° N and 30° 40′ N. Nature 344, 427–431 (1990).
- Langmuir, C. H., Bender, J. F. & Batiza, R. Petrological and tectonic segmentation of the East Pacific Rise, 5° 30′-14° 30′ N. *Nature* 322, 422-429 (1986).

 Kent, G. M. et al. Evidence from three-dimensional seismic reflectivity images for enhanced melt supply beneath mid-ocean-ridge discontinuities. *Nature* 406, 614–618 (2000).

- Carbotte, S. M., Smith, D. K., Cannat, M. & Klein, E. M. in *Magmatic Rifting and Active Volcanism* Vol. 420 (eds Wright, T. J., Ayele, A., Ferguson, D. J., Kidane, T. & Vye-Brown, C.) (The Geological Society of London, 2015).
- Lonsdale, P. Segmentation of the Pacific-Nazca Spreading Center, 1° N-20° S. J. Geophys. Res. 94, 12197–12225 (1989).
- 8. Carbotte, S. M., Small, C. & Donnelly, K. The influence of ridge migration on the magmatic segmentation of mid-ocean ridges. *Nature* **429**, 743–746 (2004).
- Toomey, D. R., Jousselin, D., Dunn, R. A., Wilcock, W. S. D. & Detrick, R. S. Skew of mantle upwelling beneath the East Pacific Rise governs segmentation. *Nature* 446, 409–414 (2007).
- 10. Bell, R. E. & Buck, W. R. Crustal control of ridge segmentation inferred from observations of the Revkianes Ridge. *Nature* **357**, 583–586 (1992).
- Weekly, R. T., Wilcock, W. S. D., Toomey, D. R., Hooft, E. E. E. & Kim, E. Upper crustal seismic structure of the Endeavour segment, Juan de Fuca Ridge from traveltime tomography: implications for oceanic crustal accretion. *Geochem. Geophys. Geosyst.* 15, 1296–1315 (2014).
- Soule, D. C., Wilcock, W. S. D., Toomey, D. R., Hooft, E. E. E. & Weekly, R. T. Near-axis crustal structure and thickness of the Endeavour segment, Juan de Fuca Ridge. *Geophys. Res. Lett.* http://dx.doi.org/10.1002/ 2016GL068182 (2016).
- 13. Gripp, A. E. & Gordon, R. G. Young tracks of hotspots and current plate velocities. *Geophys. J. Int.* **150**, 321–361 (2002).
- 14. Carbotte, S. M. \dot{et} al. Rift topography linked to magmatism at the intermediate spreading Juan de Fuca Ridge. Geology 34, 209–212 (2006).
- Ismaïl, W. B. & Mainprice, D. An olivine fabric database: an overview of upper mantle fabrics and seismic anisotropy. *Tectonophysics* 296, 145–157 (1998).
- Zhang, S. & Karato, S. Lattice preferred orientation of olivine aggregates deformed in simple shear. *Nature* 375, 774–777 (1995).
- Blackman, D. K. & Kendall, J. M. Seismic anisotropy in the upper mantle 2. Predictions for current plate boundary flow models. *Geochem. Geophys. Geosyst.* 3, 8602 (2002).
- Dunn, R. A., Toomey, D. R. & Solomon, S. C. Three-dimensional seismic structure and physical properties of the crust and shallow mantle beneath the East Pacific Rise at 9° 30′ N. J. Geophys. Res. 105, 23537–23555 (2000).
- Carbotte, S. M. et al. Variable crustal structure along the Juan de Fuca Ridge: influence of on-axis hot spots and absolute plate motions. Geochem. Geophys. Geosyst. 9, Q08001 (2008).
- Sparks, D. W. & Parmentier, E. M. Melt extraction from the mantle beneath spreading centers. *Earth Planet. Sci. Lett.* 105, 368–377 (1991).
- Dunn, R. A., Leki, V., Detrick, R. S. & Toomcy, D. R. Three-dimensional seismic structure of the Mid-Atlantic Ridge (35° N): evidence for focused melt supply and lower crustal dike injection. *J. Geophys. Res.* 110, B09101 (2005).
- Pockalny, R. A., Fox, P. J., Fornari, D. J., Macdonald, K. C. & Perfit, M. R. Tectonic reconstruction of the Clipperton and Siqueiros fracture zones: evidence and consequences of plate motion change for the last 3 Myr. *J. Geophys. Res.* 102, 3167–3181 (1997).
- 23. Sloan, H. & Patriat, P. Kinematics of the North American-African plate boundary between 28° and 29° N during the last 10 Ma: evolution of the axial geometry and spreading rate and direction. *Earth Planet. Sci. Lett.* **113**, 323–341 (1992).
- 24. Wilson, D. S. Tectonic history of the Juan de Fuca Ridge over the last 40 million years. *J. Geophys. Res.* **93**, 11863–11876 (1988).
- Bodmer, M., Toomey, D. R., Hooft, E. E. E., Nabelek, J. & Braunmiller, J. Seismic anisotropy beneath the Juan de Fuca plate system: evidence for heterogeneous mantle flow. *Geology* 43, 1095–1098 (2015).
- Pollard, D. D., Segall, P. & Delaney, P. T. Formation and interpretation of dilatant echelon cracks. Geol. Soc. Am. Bull. 93, 1291–1303 (1982).
- Morgan, J. P. & Sandwell, D. T. Systematics of ridge propagation south of 30° S. Earth Planet. Sci. Lett. 121, 245–258 (1994).
- Barth, G. A. & Mutter, J. C. Variability in oceanic crustal thickness and structure: multichannel seismic reflection results from the northern East Pacific Rise. J. Geophys. Res. 101, 17951–17975 (1996).
- Canales, J. P., Detrick, R. S., Toomey, D. R. & Wilcock, W.S. D. Segment-scale variations in the crustal structure of 150–300 kyr old fast spreading oceanic crust (East Pacific Rise, 8° 15′ N–10° 5′ N) from wide-angle seismic refraction profiles. *Geophys. J. Int.* 152, 766–794 (2003).
- Marjanovi , M., Carbotte, S. M., Nedimovi , M. R. & Canales, J. P. Gravity and seismic study of crustal structure along the Juan de Fuca Ridge axis and across pseudofaults on the ridge flanks. *Geochem. Geophys. Geosyst.* 12, 005008 (2011)
- 31. Wanless, V. D., Perfit, M. R., Klein, E. M., White, S. & Ridley, W. I. Reconciling geochemical and geophysical observations of magma supply and melt distribution at the 9° N overlapping spreading center, East Pacific Rise. *Geochem. Geophys. Geosyst.* 13, Q11005 (2012).

ARTICLES NATURE GEOSCIENCE DOI: 10.1038/NGE02745

- 32. Hooft, E. E. E., Detrick, R. S., Toomey, D. R., Collins, J. A. & Lin, J. Crustal thickness and structure along three contrasting spreading segments of the Mid-Atlantic Ridge, 33.5° –35° N. *J. Geophys. Res.* **105**, 8205–8226 (2000).
- Morgan, J. P. & Chen, Y. J. The genesis of oceanic crust: magma injection, hydrothermal circulation, and crust flow. J. Geophys. Res. 98, 6283–6297 (1993).
- Toomey, D. R. & Hooft, E. E. E. Mantle upwelling, magmatic differentiation, and the meaning of axial depth at fast-spreading ridges. *Geology* 36, 679–682 (2008).
- Sinton, J. M., Wilson, D. S., Christie, D. M., Hey, R. N. & Delaney, J. R. Petrologic consequences of rift propagation on oceanic spreading ridges. *Earth Planet. Sci. Lett.* 62, 193–207 (1983).
- Shoberg, T. & Stein, S. Investigation of spreading center evolution by joint inversion of seafloor magnetic anomaly and tectonic fabric data. *Earth Planet.* Sci. Lett. 122, 195–206 (1994).
- 37. Cormier, M. H., Scheirer, D. S. & Macdonald, K. C. Evolution of the East Pacific Rise at 16°-19° S since 5 Ma: bisection of overlapping spreading centers by new, rapidly propagating ridge segments. *Mar. Geophys. Res.* 18, 53-84 (1996).
- Bazin, S. et al. A three-dimensional study of a crustal low velocity region beneath the 9° 03′ N overlapping spreading center. Geophys. Res. Lett. 30, 111–114 (2003).
- Dunn, R. A., Martinez, F. & Conder, J. A. Crustal construction and magma chamber properties along the Eastern Lau Spreading Center. *Earth Planet. Sci. Lett.* 371–372, 112–124 (2013).
- Collier, J. S. & Sinha, M. C. Seismic mapping of a magma chamber beneath the Valu Fa Ridge, Lau Basin. J. Geophys. Res. 97, 14031–14053 (1992).
- Kent, G. M., Harding, A. J. & Orcutt, J. A. Distribution of magma beneath the East Pacific Rise between the Clipperton Transform and the 9° 17′ N deval from forward modeling of common depth point data. *J. Geophys. Res.* 98, 13945–13969 (1993).
- 42. Nedimovi , M. R. et~al. Frozen magma lenses below the oceanic crust. *Nature* **436**, 1149–1152 (2005).
- Crawford, W. C. & Webb, S. C. Variations in the distribution of magma in the lower crust and at the Moho beneath the East Pacific Rise at 9°-10° N. Earth Planet. Sci. Lett. 203, 117-130 (2002).
- 44. Zha, Y. *et al.* Seismological imaging of ridge–arc interaction beneath the Eastern Lau Spreading Center from OBS ambient noise tomography. *Earth Planet. Sci. Lett.* **408**, 194–206 (2014).
- Neumann, G. A. & Forsyth, D. W. The paradox of the axial profile: isostatic compensation along the axis of the Mid-Atlantic Ridge? *J. Geophys. Res.* 98, 17891–17910 (1993).

- 46. Cannat, M. How thick is the magmatic crust at slow spreading oceanic ridges? *J. Geophys. Res.* **101**, 2847–2857 (1996).
- 47. Magde, L. S. & Sparks, D. W. Three-dimensional mantle upwelling, melt generation, and melt migration beneath segment slow spreading ridges. *J. Geophys. Res.* **102**, 20571–20583 (1997).
- 48. White, S. M., Haymon, R. M., Fornari, D. J., Perfit, M. R. & Macdonald, K. C. Correlation between volcanic and tectonic segmentation of fast-spreading ridges: evidence from volcanic structures and lava flow morphology on the East Pacific Rise at 9°–10° N. J. Geophys. Res. 107, B8–2173 (2002).
- 49. Aghaei, O. *et al.* Crustal thickness and Moho character of the fast-spreading East Pacific Rise from 9° 42′ N to 9° 57′ N from poststack-migrated 3-D MCS data. *Geochem. Geophys. Geosyst.* **15**, 634–657 (2014).
- Karsten, J. L., Delaney, J. R., Rhodes, J. M. & Liias, R. A. Spatial and temporal evolution of magmatic systems beneath the Endeavour segment, Juan de Fuca Ridge: tectonic and petrologic constraints. *J. Geophys. Res.* 95, 19235–19256 (1990).

Acknowledgements

We thank the officers and crew of the RV *Marcus G. Langseth* as well as the OBS teams from Scripps Institution of Oceanography and Woods Hole Oceanographic Institution for their assistance in the acquisition of the seismic data. Additional assistance was provided by onboard passive acoustic technicians and marine mammal observers to ensure that data collection was accomplished in compliance with guidelines set forth by marine environmental assessments and permits. The experiment and analysis were supported by the NSF under grants numbered OCE-0454740 to the University of Washington and OCE-0454747 and OCE-0651123 to the University of Oregon.

Author contributions

D.R.T., E.E.E.H. and W.S.D.W. designed the experiment and participated in data collection and processing. B.P.V. conducted the tomographic analysis. B.P.V. and D.R.T. wrote the initial manuscript with comments from co-authors. All authors discussed the results and their implications and assisted in revising the manuscript.

Additional information

Supplementary information is available in the online version of the paper. Reprints and permissions information is available online at www.nature.com/reprints. Correspondence and requests for materials should be addressed to B.P.V.

Competing financial interests

The authors declare no competing financial interests.

NATURE GEOSCIENCE DOI: 10.1038/NGE02745 ARTICLES

Methods

Data and starting model. We use the arrival times of mantle refractions (Pn) that undershoot the ridge axis to tomographically image the uppermost mantle. These data are picked on the outermost shot lines and ocean-bottom seismometers (OBSs; each instrument is equipped with three orthogonal geophones and a hydrophone) that make up the Endeavour Tomography (ETOMO) experiment (Supplementary Fig. 1). The well-tuned airgun array of the RV Marcus G. Langseth provided an impulsive seismic source that allows us to pick Pn travel-times with low uncertainty. To further enhance data quality, we summed the vertical and hydrophone channels where good quality data were recorded on both components. A total of 5,528 handpicked Pn arrivals with a mean mean travel-time uncertainty of 11 ms are included in our tomographic inversion. The uncertainties were estimated visually on the basis of the impulsiveness of the Pn arrival and the trace-to-trace coherency of waveforms. Additional sources of error affecting travel-time picks include source and receiver location uncertainties, instrument clock corrections, and uncertainties in bathymetry. These experimental errors are typically smaller than the picking error^{11,51}. To ensure only mantle refractions are included in our data set, we include only picks with source-receiver offsets greater than 40 km. Supplementary Fig. 2 shows Pn arrivals and travel-time picks from the shot line and OBS identified in Supplementary Fig. 1.

Previous tomographic analysis of 96,156 crustal refractions (Pg; ref. 11) and 22,577 Moho reflections (PmP; ref. 12) provides a 3D starting model of crustal velocity and thickness. These studies incorporated data from both the outermost experimental grid and a denser grid of airgun shots and OBSs centred along the ridge axis (Supplementary Fig. 1). As a result, structure along the crustal legs of Pn ray paths is well constrained (Supplementary Fig. 3) and variations in Pn travel-times largely reflect mantle structure⁵².

Azimuthal anisotropy. We use azimuthal variations in Pn travel-time residuals to identify the segment-scale anisotropic structure. Weak upper mantle anisotropy is well approximated by a hexagonal symmetry system with an axis of symmetry (the fast direction of P-wave propagation) oriented sub-parallel to the horizontal plane 53,54 . Under this approximation, P-wave velocity varies azimuthally as a periodic function of 2θ and 4θ terms, where θ is the source–receiver azimuth with respect to the spreading direction 55,56 . Assuming a homogeneous mantle anisotropic structure, this gives rise to a sinusoidal pattern in arrival time delays (Δt) , which can be parameterized as follows:

$$\Delta t = \alpha_0 + \alpha_1 \cos(2\theta) + \alpha_2 \sin(2\theta) + \alpha_3 \cos(4\theta) + \alpha_4 \sin(4\theta)$$

where α_0 is the mean delay and α_1 , α_2 , α_3 and α_4 control the magnitude and orientation of mantle anisotropy. The amplitude (A_n) and phase (ψ_n) of the 2θ (n=2) and 4θ (n=4) terms are defined as follows:

$$A_n = \sqrt{\alpha_{n-1}^2 + \alpha_n^2}$$

$$\psi_n = \operatorname{atan}\left(\frac{\alpha_n}{\alpha_{n-1}}\right)$$

Standard errors (s_z) in the amplitude and phase are estimated using the Gaussian error propagation rule⁵⁷:

$$s_z = \sqrt{\left(\frac{\partial z}{\partial \alpha_1} s_{\alpha_1}\right)^2 + \left(\frac{\partial z}{\partial \alpha_2} s_{\alpha_2}\right)^2}$$

where z is the amplitude or phase. In mantle rocks, the 4θ terms are predicted to be much smaller than the 2θ terms 56 and so we choose to set α_3 and α_4 to zero. This choice is justified by our data. Attempting to fit all five free parameters does not significantly alter the magnitude or the fast-axis orientation relative to fitting only 2θ terms. This is because the amplitudes of the best-fit 4θ terms are an order of magnitude smaller than the 2θ terms. Furthermore, the standard errors in the α_3 and α_4 parameters are of the same order as the parameter values themselves, indicating that they are not required to fit our Pn data set.

We determine the coefficients α_0 , α_1 and α_2 using a weighted least-squares fit to the Pn travel-time residuals. Delays are calculated with respect to an isotropic, homogeneous (7.6 km s⁻¹) mantle and corrected to a common range (40 km) based on the mantle path length. To reduce the effects of isotropic heterogeneity in our estimate of anisotropy, we bin the Pn delays and fit the mean delay in each bin. Errors in the mean delay of each bin are estimated using a Student's t-test with a 95% confidence interval. These errors are used to weight the least-squares fit.

We made many estimates of anisotropy across a range of bin sizes and data subsets, all of which indicate clockwise rotation in the fast direction of mantle anisotropy with respect to the plate-spreading direction (110°; ref. 13). We present two anisotropic models in Supplementary Fig. 4a,b. The first model includes all 5,528 Pn delays binned at 10° (Supplementary Fig. 4a) and has a best-fit fast-axis orientation of $127^{\circ} \pm 1^{\circ}$ and a magnitude of $3.9 \pm 0.5\%$; relative to the plate-spreading direction, the fast axis is skewed clockwise by 17° . To remove

potential complexities associated with the OSCs, where isotropic heterogeneity is particularly pronounced (Fig. 2b), a second model is presented (Fig. 3 and Supplementary Fig. 4b) in which we removed all Pn delays associated with ray paths that pass beneath overlapping portions of the ridge (a total of 1,232 delays are removed). This second anisotropic model has a best-fit orientation of $122^{\circ}\pm 1^{\circ}$ and magnitude of $4.7\pm 0.4\%$; relative to the plate-spreading direction, the fast axis is skewed clockwise by 12° . We note that a homogeneous anisotropic structure alone explains greater than 40% of the data variance, indicating that seismic anisotropy is a robust signal in our data. In addition to estimating mantle anisotropy by analysing travel-time delays, we also performed grid-search inversions over various anisotropic models (see the Model sensitivity section). These results are consistent with the anisotropic structure interpreted from azimuthal variations in Pn delays, in particular, the subset of Pn data that does not include paths beneath the OSCs. On the basis of these analyses, we imposed the anisotropic structure presented in Fig. 3 and Supplementary Fig. 4b to construct our preferred tomographic solution.

We also verified that our estimate of anisotropy is not an artefact of the Pn ray geometry or likely heterogeneity in the isotropic structure. To do this we created synthetic Pn travel-times for a model that included our preferred mantle isotropic structure (Fig. 2b) and 4% mantle anisotropy with the fast-axis oriented parallel to the plate-spreading direction (110°; ref. 13). Random noise with a standard deviation of 11 ms was added to the synthetic travel-times. We then determined the best-fit anisotropic model following the methods described above. Fitting all synthetic Pn delays, including those that sample the overlapping ridges, the best-fit anisotropic model has a fast-axis orientation of $112^{\circ} \pm 1^{\circ}$ and a magnitude of $3.6 \pm 0.4\%$ (Supplementary Fig. 4c). The fast-axis orientation is slightly overestimated in the clockwise direction and the magnitude of anisotropy is within the standard error. Fitting only those synthetic Pn delays that travel beneath the non-overlapping sections of the Endeavour segment results in a best-fit fast-axis orientation of $110^{\circ} \pm 1^{\circ}$ and magnitude of $5.2 \pm 0.4\%$ (Supplementary Fig. 4d). This subset of Pn delays accurately determines the fast-axis orientation but over predicts the magnitude by \sim 1%. We conclude from these tests that the anisotropic models predicted from fitting Pn travel-time residuals are not significantly influenced by likely heterogeneity in isotropic structure or ray path coverage.

Tomographic procedure. We use an iterative tomographic technique in which travel-time residuals are inverted for 3D slowness (that is, inverse of velocity) perturbations^{21,58}. Ray paths and travel-times are predicted using a shortest path algorithm⁵⁹. Ray tracing is performed on a 3D grid parameterized in terms of anisotropic slowness²¹ and includes seafloor topography⁵⁸. Anisotropic slowness (*u*) is parameterized assuming a hexagonal symmetry system and is defined as:

$$u(\mathbf{r}) = \frac{u_{iso}(\mathbf{r})}{1 + A(\mathbf{r})\cos[2\theta(\mathbf{r})] + B(\mathbf{r})\sin[2\theta(\mathbf{r})]}$$

where u_{iso} is the isotropic slowness at position r, θ is the ray azimuth measured from the x axis, and A and B are scale terms that control the magnitude and orientation of the fast axis of seismic anisotropy defined as $2\sqrt{A^2+B^2}$ and 0.5atan(B/A), respectively. For the forward problem, we use a grid spacing of 200 m in the x-, y- and z-directions. The inversion volume extends 90 km in the cross-axis direction, 120 km in the ridge-parallel direction, and 11 km beneath the seafloor (Supplementary Fig. 1).

The inverse problem is regularized with smoothing and damping constraints requiring the user to specify a priori smoothing parameters and model uncertainties. We chose to minimize a function of the form:

$$\begin{split} s^2 &= \Delta t' C_{\rm d}^{-1} \Delta t + \lambda_{\rm p} (m_0 + \Delta m)' C_{\rm m}^{-1} (m_0 + \Delta m) \\ &+ \lambda_{\rm v} (m_0 + \Delta m)' C_{\rm v}^{-1} (m_0 + \Delta m) + \lambda_{\rm h} (m_0 + \Delta m)' C_{\rm h}^{-1} (m_0 + \Delta m) \end{split}$$

where Δt is a vector containing the differences between observed and predicted travel-times; $C_{\rm d}$ is a diagonal matrix containing the data variance defined by the squared travel-time uncertainties; $m_{\rm o}$ is a vector of the cumulative perturbation to the isotropic and anisotropic model parameters from previous iterations; Δm is the model perturbation for the current iteration; $C_{\rm m}$ is a diagonal matrix containing the a priori model variance; $C_{\rm v}$ and $C_{\rm h}$ are matrices that apply vertical and horizontal nearest-neighbour smoothing, respectively, to each model parameter; and $\lambda_{\rm p}$, $\lambda_{\rm v}$ and $\lambda_{\rm h}$ are weighting parameters that set the relative importance of damping, vertical smoothing and horizontal smoothing constraints, respectively. The perturbational model for isotropic slowness is gridded at 1 km intervals in the x, y and z directions. With nearest-neighbour smoothing constraints, this grid spacing results in slowness perturbations that are smoothed over a volume comparable to that of the first mantle Pn Fresnel volume, which defines the theoretical limit of our spatial resolutions 52 . We assess the model fit to the observed travel-times and compare alternative solutions using the following metric:

$$\chi^2 = \frac{1}{N} \sum_{i=1}^{N} \frac{\Delta t_i^2}{\sigma_i^2}$$

ARTICLES NATURE GEOSCIENCE DOI: 10.1038/NGE02745

where N is the number of travel-time residuals and Δt_i and σ_i are the travel-time residual and pick error for the ith observation, respectively. Values of $\chi^2 < 1$ suggest that the model is overfitting the data and values of $\chi^2 > 1$ suggest that the model is underfitting the data. We seek solutions that are spatially smooth, limit the norm of the perturbational model vector, and attain a χ^2 reasonably close to unity.

Our preferred model was obtained with $\lambda_v = \lambda_h = 200$, $\lambda_p = 1$, and depth-dependent slowness uncertainties increasing from 1% in the upper crust to 50% in the mantle. Crustal uncertainties are taken to be small since the 3D crustal structure and thickness is constrained by previous work^{11,12}. The Pn ray paths sample a depth range between 6.5 and 8 km beneath the seafloor and because their Fresnel zone is approximately 2 km in the vertical dimension we cannot resolve vertical variations in structure beneath the Moho. Therefore, we chose a vertical smoothing value such that model perturbations do not vary significantly with depth beneath the Moho (Supplementary Fig. 5). We display our preferred solution at 7.8 km beneath the seafloor (Fig. 2b), which is the shallowest seafloor-conformable depth that is entirely within the mantle (Supplementary Fig. 5a,b). A map view section that is conformable to the Moho surface is effectively identical (Supplementary Fig. 5c). We searched over various horizontal smoothing values and chose that which provided a smooth solution that fit the data well. Travel-time calculations and inversion for model parameters were performed until the root mean square (r.m.s.) travel-time residual converged (typically 4–5 iterations). Our preferred model converged to a χ^2 -misfit of 1.06 and r.m.s. travel-time residual of 11 ms after 4 iterations (Supplementary Fig. 6).

Model sensitivity. We performed numerous inversions to test the stability of our result with respect to inversion parameters, perturbational grid size, and the starting mantle and crustal velocity models. In general, decreased smoothing and damping constraints and finer perturbation grids result in higher magnitude, shorter wavelength perturbations while increased smoothing and damping constraints, and coarser perturbation grids result in lower magnitude and smoother perturbations. Changes to the initial isotropic mantle velocity produced effectively identical mantle images. The main features of our preferred model, anomalously broad and high-magnitude MLVZs beneath the OSCs and a narrower region of low velocities beneath the segment centre, were consistently observed in all of our tomographic solutions.

To examine the trade-off between isotropic and anisotropic structure we performed a series of grid-search inversions over starting models with fixed anisotropy orientations. A clear minimum in the χ^2 -misfit is observed when the fast-axis orientation matches that fit to the Pn travel-time residuals (Supplementary Fig. 7), which is rotated 12° clockwise from the plate-spreading direction. The grid-search results presented in Supplementary Fig. 7 were performed with a magnitude of anisotropy of 4.7% (that is, the best-fit magnitude determined from travel-time residuals). Similar curves are obtained when imposing a magnitude of anisotropy of 3.5% and 6% (Supplementary Fig. 7). However, at these magnitudes the model misfit is systematically greater compared with the best-fit magnitude. Imposing an isotropic mantle resulted in a significantly increased χ^2 -misfit (1.62) substantiating the presence of mantle anisotropy. Limited azimuthal coverage and strong isotropic heterogeneity prevented a robust interpretation of mantle anisotropy beneath overlapping portions of the Endeavour from travel-time residuals alone. To determine whether anisotropic structure is required beneath the segment ends, we inverted our Pn data set assuming only the mantle beneath the central, non-overlapping, portion of the Endeavour is seismically anisotropic. This resulted in an increased χ^2 -misfit (1.14), suggesting that the mantle beneath the entire length of the Endeavour is seismically anisotropic.

To test the sensitivity of our preferred solution to the starting crustal thickness model, we inverted the Pn arrival times under the assumption that crustal thickness does not vary, which is a poor assumption given previous studies at Endeavour^{12,19} and elsewhere along the JdFR^{19,30} and EPR^{28,29}. We created a model with uniform crustal thickness of 6.8 km (the mean value of the tomographically determined crustal thickness model¹²) and inverted our Pn data set for isotropic perturbations. We assumed our preferred anisotropic model and followed the inversion procedure outlined above. The recovered isotropic structure (Supplementary Fig. 8a) is comparable to our preferred results (Fig. 2b and Supplementary Fig. 5). In particular, the MLVZ is relatively narrow beneath the central region of the Endeavour segment and anomalously wide beneath each OSC. The primary effect of assuming constant crustal thickness is to decrease the amplitude of the low-velocity anomalies beneath each OSC. This occurs because the assumed crustal thickness (6.8 km) overestimates the thickness of the crust beneath each OSC by 0.5-0.8 km. We also verified that the anisotropic structure interpreted from Pn delays is insensitive to crustal thickness variations. We calculated azimuthal variations in Pn travel-times relative to a model with constant crustal thickness (6.8 km) and an isotropic, homogeneous (7.6 km s⁻¹) mantle (Supplementary Fig. 8b). These residuals are processed and fit following the same procedure used to construct our preferred anisotropic model. The best-fit fast-axis

orientation and magnitude is $125^{\circ}\pm1^{\circ}$ (15° clockwise from the plate-spreading direction) and $4.7\%\pm0.4\%$, respectively. This result is nearly identical to our preferred estimate of mantle anisotropy. We conclude that the mantle isotropic and anisotropic structure is relatively insensitive to crustal thickness variations.

Model resolution. We identify the region in which our preferred model is well resolved by analysing the spatial distribution of ray paths. Specifically, we use the derivative weight sum (DWS) to measure the density of predicted ray paths that influence each perturbational node in the inversion volume 60 . On the basis of chequerboard resolution tests (discussed below), anomalies located within regions of the model space with a DWS less than $\sim\!30$ are poorly reconstructed. Therefore, we mask regions of the model with a DWS below 30. The vast majority of mantle perturbational nodes within 20 km of the plate boundary have a DWS value greater than 1,000 (Supplementary Fig. 9a).

We assess the resolution of mantle isotropic structure using chequerboard tests. We constructed synthetic models with an alternating sinusoidal pattern of positive and negative isotropic velocity anomalies with a magnitude of 5% applied to a homogeneous mantle with velocity of 7.6 km s⁻¹. Each anomaly covered a 10 km by 10 km square region in the x-y plane and the polarity of the anomalies did not vary with depth. No anomalies were placed within the crust and we imposed 4% mantle anisotropy with a fast axis rotated 12° clockwise from the plate-spreading direction. We calculated travel-times for Pn arrivals using the same data geometry used to construct our preferred solution. Each travel-time was assigned an uncertainty of 11 ms and random noise with a standard deviation of 11 ms was added to the synthetic Pn data set. These travel-times were then inverted for isotropic perturbations (the true anisotropic structure was assumed for the starting model) following the same inversion procedure used in our preferred solution. The results of this test are shown in Supplementary Fig. 9b. In general, the distribution of recovered mantle perturbations accurately reflects the true chequerboard model. The locations of low-velocity anomalies are well recovered while the magnitudes are typically underestimated. Our chequerboard tests indicate that mantle structure is well constrained within \sim 20 km of the plate boundary and beneath each OSC.

In addition to chequerboard tests, we assess our model resolution by reconstructing more geologically plausible anomalies. We constructed a synthetic model containing three circular low-velocity anomalies, 5 km in diameter, along the segment centre. We also placed two circular low-velocity anomalies, 10 km in diameter, beneath either OSC. The magnitude of all five MLVZs is 5% with respect to a 7.6 ${\rm km}\,{\rm s}^{-1}$ mantle and each anomaly extends from the Moho to the base of our model. Synthetic arrival times were created, processed and inverted the same as for the chequerboard test described above. The true and recovered models are shown in Supplementary Fig. 9c. The locations of all five anomalies are accurately recovered and, as is common in tomography, the magnitudes of the low-velocity anomalies are underestimated by \sim 1–2%. As a consequence of the smoothing constraints required to regularize the inverse problem, the spatial extent of each anomaly is overestimated by at most a few kilometres. We conclude from this resolution test that the broad MLVZs beneath the OSCs observed in our preferred tomographic solution (Fig. 2b) are a robust feature and that velocity anomalies as small as \sim 5 km in diameter are resolved by our Pn data set.

Code availability. The computer code associated with this paper is maintained by D.R.T. at the University of Oregon (drt@uoregon.edu). Some components are available on request.

Data availability. The ETOMO seismic data set is available on request through the IRIS-DMC (report number 09-014; http://ds.iris.edu/ds/nodes/dmc). The ETOMO cruise report can be accessed at http://pages.uoregon.edu/drt/MGL0910_Science_Report.

References

- Barclay, A. H., Toomey, D. R. & Solomon, S. C. Seismic structure and crustal magmatism at the Mid-Atlantic Ridge, 35° N. J. Geophys. Res. 103, 17827–17844 (1998).
- Zhang, Z., Shen, Y. & Zhao, L. Finite-frequency sensitivity kernels for head waves. *Geophys. J. Int.* 171, 847–856 (2007).
- Nicolas, A. & Christensen, N. I. in Composition, Structure and Dynamics of the Lithosphere-Asthenosphere System (eds Fuchs, K. & Froidevaux, C.) 111–123 (American Geophysical Union, 1987).
- Becker, T. W., Chevrot, S., Schulte-Pelkum, V. & Blackman, D. K. Statistical properties of seismic anisotropy predicted by upper mantle geodynamic models. *J. Geophys. Res.* 111, B08309 (2006).
- Backus, G. E. Possible forms of seismic anisotropy of the uppermost mantle under oceans. J. Geophys. Res. 70, 3429–3439 (1965).
- Shearer, P. M. & Orcutt, J. A. Compressional and shear wave anisotropy in the oceanic lithosphere-the Ngendei seismic refraction experiment. *Geophys. J. Int.* 87, 967–1003 (1986).

NATURE GEOSCIENCE DOI: 10.1038/NGE02745 ARTICLES

- 57. Taylor, J. R. An Introduction to Error Analysis: The Study of Uncertainties in Physical Measurements (University Science Books, 1994).
- 58. Toomey, D. R., Solomon, S. C. & Purdy, G. M. Tomographic imaging of the shallow crustal structure of the East Pacific Rise at 9° 30' N. J. Geophys. Res. 99, 24135–24157 (1994).
- Moser, T. J. Shortest path calculation of seismic rays. Geophysics 56, 59–67 (1991).
- Toomey, D. R. & Foulger, G. R. Tomographic inversion of local earthquake data from the Hengill-Grensdalur Central Volcano Complex, Iceland. *J. Geophys.* Res. 94, 17497–17510 (1989).